**Supporting Information**

# Synergistic light management and interface engineering of $SnO_2$ for scalable, high-performance air-processed perovskite solar cells

Bowen Li[1, 6], Yiming Liu[1, 6], Ziwei Zheng[2, 6], Yequan Xiao[1*], Chunxiang Lan[3], Tian Zhang[3], Li Guan[4], Peng Xiang[1], Rui Guo[2], Yingying Shi[3], Miaomiao Zeng[3], Kunyuan Zheng[1], Pengfei Liu[1], Hao Xiong[1], Yiteng Tu[1], Jing Guo[2, 5*], Xiong Li[2, 3*] and Xinyu Tan[1*].

[1] Hubei Provincial Engineering Research Center for Solar Energy High-value Utilization and Green Conversion, College of Materials Science and Engineering, College of Electrical Engineering & New Energy, China Three Gorges University Yichang, Hubei 443002, P. R. China.

[2] School of Physics and Optoelectronic Engineering, Hainan University, Haikou, 570228, P. R. China

[3] Michael Grätzel Center for Mesoscopic Solar Cells, Wuhan National Laboratory for Optoelectronics, Huazhong University of Science and Technology, Wuhan 430074, Hubei, P. R. China.

[4] Department of Physics Science and Technology, Hebei University, Baoding, 071000, P. R. China

[5] Center for Advanced Studies in Precision Instruments, Hainan University, Haikou, 570228, P. R. China

[6] These authors contributed equally: Bowen Li, Yiming Liu, Ziwei Zheng.

***Corresponding authors:**

Email: xiaoyequan@ctgu.edu.cn (Yequan Xiao); guojing@hainanu.edu.cn(Jing Guo)；

xiongli@hust.edu.cn (Xiong Li); tanxin@ctgu.edu.cn (Xinyu Tan).

## Methods

### Chemicals

The $SnO_2$ nanoparticle precursor (tin (IV) oxide, 15% in $H_2O$ colloidal dispersion), L-histidine (His) and L-Histidine monohydrate monohydrochloride (His-HCl·$H_2O$) were purchased from Alfa Aesar. DI water, dimethylformamide (DMF), dimethyl sulfoxide (DMSO), chlorobenzene (CB), isopropanol (IPA), acetonitrile (ACN) and benzotrifluoride (TFMB) were purchased from Thermo Fisher. Lead iodide ($PbI_2$), lead chloride ($PbCl_2$), cesium Iodide (CsI), formamidinium iodide (FAI), methylammonium chloride (MACl), 4-tertbutylpyridine (tBP), bis (triflfluoromethane) sulfonamide lithium salt (Li-TFSI), and(2,2',7,7'-tetrakis(N,N-di-p-methoxyphenylamino)-9,9'-spirobifluorene (Spiro-OMeTAD) were purchased from Advanced Election Technology Co,. Ltd. (China). 4-Methoxyphenethylammonium Iodide (p-MeOPEAI) was purchased from Xi'an Polymer Light Technology Corp (China). Au pellets were purchased from Liaoning Huite Optoelectronic Technology Co., Ltd.

### Fabrication of NC-$SnO_2$ layer

The ITO substrate was cleaned by sonicating in Hellmanex solution, DI water, EtOH, and IPA for 15 min each. The NC-$SnO_2$ (4.4mg $mL^{-1}$; pH $\approx$ 7.5) precursor was prepared by mixing 528 μL of His-HCl·$H_2O$ solution in water (10mg $ml^{-1}$), 472 μL of $H_2O$, 200 μL of $SnO_2$ nanoparticle precursor. Regarding 4.0 mg $mL^{-1}$ and 4.8 mg $mL^{-1}$ NC-$SnO_2$, the His-HCl·$H_2O$ aqueous solution was adjusted to 480 μL and 576 μL, and the corresponding $H_2O$ was adjusted to 520 μL and 424 μL respectively, the $SnO_2$ nanoparticle precursor was maintained at 200 μL. The precursor should be stirred well for at least 2 hours before use. The NC-$SnO_2$ precursor was deposited via spin coating at 5000 rpm for 30 seconds (3000 rpm ramp). In particular, we recommend loading the fresh NC-$SnO_2$ precursor into a syringe equipped with a 0.22 μm PTFE filter, spreading the precursor directly on the ITO glass via the syringe and then spin coating. The

ITO/$SnO_2$ substrate was annealed in an ambient environment (RH ≈ 35%) at 150 °C for 30 min and oxygen plasma treated.

For the conventional ETL, $SnO_2$ nanocrystal colloidal solution was using diluted $SnO_2$ nanoparticle solution ($SnO_2$ nanoparticle precursor:DI water = 1:5). The other preparation procedures were consistent with the NC-$SnO_2$ layer.

Device fabrication

Before spin coating the perovskite, we transferred the ITO/$SnO_2$ substrate to a humidity-controlled air environment (RH≤5%). We used an $FA_{0.95}Cs_{0.05}PbI_3$ perovskite composition with excess $PbI_2$ and $PbCl_2$ stoichiometry (3 mol% and 6 mol%), the perovskite solution was prepared by mixing 1.442 M $PbI_2$, 0.084 M $PbCl_2$,1.33 M FAI, 0.07 M CsI and 0.42 M MACl in DMF:DMSO=4:1. The perovskite solution was deposited via spin coating at 4500 rpm for 25 seconds (1500 rpm ramp). At 17 s, 150 μL of mixed antisolvent (CB:TFMB = 95:5) was deposited onto the substrate. Next, the substrate with wet perovskite film was quickly transferred to RH≈35% air for annealing at 150℃ for 20min. For the 2D perovskite passivation, 40 μL of p-MeOPEAI (2mg/mL in IPA) was deposited at 5000 rpm for 30 sec and annealed at 100 °C for 5 min. The hole transporting layer (HTL) was deposited by preparing the HTL solution according to the Li-TFSI doped Spiro-OMeTAD. Conventionally, 72.3 mg of Spiro-OMeTAD, 17.5 μL Li-TFSI stock solution (520 mg Li-TFSI in 1 mL ACN), 28.8 μL tBP were added in 1 ml of CB. The HTL solution was spin-coated at 4000 rpm for 30 sec with a ramp of 2000 rpm/sec. The p-MeOPEAI and HTL solution deposition were performed in an air environment with a humidity of≤5%. The Au electrode (80 nm) was deposited by thermal evaporation.

Module fabrication

The perovskite solar module consisted of six perovskite sub-cells connected in series on a 6 cm ×6 cm substrate. Between each sub-cell, P1 line was laser-scribed (20 W, 1064 nm, 30 kHz) with a width of ~100 μm. The ETL, perovskite and HTL were prepared with the same process as used for cell fabrication. After depositing the ETL,

perovskite layer and HTL, P2 line with a width ~100 μm was laser-scribed. Finally, a gold electrode with a thickness of 80 nm was deposited by thermal evaporation, and etched by mechanical scribing (P3, width ~100 μm) to form the typical series-connection of PSMs [1,2].

Device Characterization

Current density-voltage (*J-V*) curves were recorded using a solar simulator (Newport, Oriel Class AAA, 91195A) and a source meter (Keithley 2400). The illumination was set to AM1.5G and calibrated to 100 mW/cm$^2$ using a calibrated silicon reference cell. The step voltage was 10 mV. The active area was controlled by using a dark mask with a defined aperture. External Quantum Efficiency (EQE) is measured using a lab-built system with a monochromator, 150W Xenon-arc lamp (model 66902), an mHz-kHz Chopper Controller (model 75160), and a Merlin lock-in detector (model 70105) from Newport Optical Instruments U.S.A. Before each measurement, the system is calibrated with a Si photodiode from Thorlabs (FDS1010) under 300-900 nm wavelength. Experimental data is then acquired with an interval wavelength of 5 nm and a time delay of 100 ms. The operational stability tests were carried out at the maximum power point (MPP) for the unencapsulated cells under AM 1.5G 1 sun continuous illumination in nitrogen ($N_2$) atmosphere which was produced by a LED-lamp-based solar simulator. The surface temperature of cells was controlled to be 30±3 °C. The bias at the MPP was calculated and applied automatically. The light intensity was calibrated by a standard silicon reference cell from Newport.

Grazing Incidence Wide Angle X-ray Scattering (GIWAXS)

The GIWAXS measurements were performed at BL03HB beamline of the Shanghai Synchrotron Radiation Facility (SSRF). X-ray with a wavelength of 1.238 Å was utilized for incident-angle-depending measurements, and the incident angle was fixed at 0.2° and 0.6°.

Dynamic Light Scattering (DLS) measurement

The particle size information of $SnO_2$, His-$SnO_2$ and NC-$SnO_2$ precursors after sufficient stirring was tested using a DLS particle size analyzer (Malvern; Zetasizer Nano ZS).

Scanning Electron Microscopy (SEM)

SEM images were recorded using a Nova Nano SEM 450 FP2053/45 in the HUST. Optoelectronic micro&nano fabrication and characterizing facility.

AFM and c-AFM measurements

The $\omega_0$ resonance frequency and spring constant of the AFM probe are approximately 75 kHz and 2.8 N $m^{-1}$. For the c-AFM mode, it is based on the contact mode. At the same time, a 500 mV bias is applied, the sample stage is grounded, and the current passes through the probe and the feedback loop to form a current graph.

Optical index (*n*, *k* value) measurements

The measurements of refractive index (*n* value) and extinction coefficient (*k* value) were recorded using a Ellipsometer (RC2, J. A. WOOLLAM) in the HUST. Optoelectronic micro&nano fabrication and characterizing facility, and the thickness of the film was calibrated by cross-sectional SEM and step profiler.

Reflectivity measurement

The reflectivity of Glass/ITO/$SnO_2$, His-$SnO_2$ or NC-$SnO_2$/PVSK was measured using a UV/Vis/NIR Spectrophotometer (PerkinElmer; Lambda 1050+) in the HUST. Optoelectronic micro&nano fabrication and characterizing facility, with glass on the incident side, and the average transmittance under the AM1.5G spectrum was calculated.

The average transmittance in the wavelength range $\lambda_1$-$\lambda_2$ and visible light can be calculated by the following equation [3-5]:

$$\overline{T}_{(\lambda_1-\lambda_2)} = \frac{\int_{\lambda_1}^{\lambda_2} \tau(\lambda) I_{AM.1.5G}(\lambda) d\lambda}{\int_{\lambda_1}^{\lambda_2} I_{AM.1.5G}(\lambda) d\lambda}, \quad (1)$$

$$\overline{T}_{VIS} = \frac{\int_{400nm}^{800nm} \tau(\lambda) I_{AM.1.5G}(\lambda) d\lambda}{\int_{400nm}^{800nm} I_{AM.1.5G}(\lambda) d\lambda}, \quad (2)$$

here, $\overline{T}_{(\lambda_1\text{-}\lambda_2)}$ is the transmittance of sample, a weighted average value. $\lambda$ is the wavelength. $\tau(\lambda)$ is the transmittance of sample. $I_{\text{AM.1.5}}(\lambda)$ represents the solar illumination of the AM 1.5 spectrum. d$\lambda$ is wavelength interval. $\overline{T}_{\text{VIS}}$ is the average visible light transmittance.

The average solar reflectance ($\overline{R}_{\text{Solar}}$) is defined as shown in equation (3):

$$\overline{R}_{Solar} = \frac{\int_{0.3\mu m}^{2.5\mu m} I_{Solar}(\lambda) R(\lambda) d\lambda}{\int_{0.3\mu m}^{2.5\mu m} I_{Solar}(\lambda) d\lambda}, \quad (3)$$

where $\lambda$ is the solar wavelength, $I_{\text{Solar}}(\lambda)$ is the normalized ASTM G173 global solar spectrum, and $R(\lambda)$ is the sample's spectral reflectance. Similarly, the thermal emittance $\overline{\varepsilon}_{(\lambda_1\text{-}\lambda_2)}$is defined as shown in equation (4):

$$\overline{\varepsilon}_{(\lambda_1-\lambda_2)} = \frac{\int_{\lambda_1}^{\lambda_2} I_{bb}(T,\lambda)\overline{\varepsilon}(T,\lambda) d\lambda}{\int_{\lambda_1}^{\lambda_2} I_{bb}(T,\lambda) d\lambda}, \quad (4)$$

where $\overline{\varepsilon}(T,\lambda)$ is the sample's spectral emittance and $I_{bb}(T,\lambda) = \frac{2c^2h}{\lambda^5} \frac{1}{e^{\frac{hc}{\lambda k_B T}} - 1}$ is indicating the solar intensity of the blackbody at the temperature $T$ [6].

Fourier transform infrared (FTIR)

Infrared absorption spectra of the samples were collected using an FT-IR Spectrometer (VERTEX 80v, Bruker) with a collimated UltraScan interferometer, collecting spectra at a spectral resolution of 0.06 cm-1.

XPS and UPS measurements

X-ray photoelectron spectra (XPS) and ultraviolet photoelectron spectra (UPS) measurements were carried out on a Thermo-Fisher ESCALab 250Xi system with a monochromatized Al Kα (for XPS mode) under the pressure of 5.0×10-7 Pa.

Kelvin probe force microscopy (KPFM) measurement

Kelvin probe force microscopy (KPFM) measurements were conducted using an atomic force microscopy measurement system (Flex-Mount, Nanosurf).

Photoluminescence (PL) spectroscopy measurement

PL spectra were collected thought a Raman spectrometer (LabRAM HR Evolution, France) under an excitation of 532 nm.

TPV and TPC measurements

TPV and TPC measurements were performed as follows: the devices were illuminated with a laser pulses (532 nm, 100 mJ, 6 ns width from an Nd:YAG laser), and then the decay of signals was collected through a 1 GHz Agilent digital oscilloscope (DSO-X3102A) with the input impedance of 1 MΩ/50 Ω.

The Space-Charge-Limited Current (SCLC) measurements

The SCLC devices were fabricated with the structure of ITO/$SnO_2$/PVSK/$PC_{61}BM$/$C_{60}$/BCP/Ag and measured under dark at room temperature with Keithley 2400 Source Meter.

TRPL and TRPL mapping measurements

The images were obtained using a mercury lamp (U-LH100HG, Olympus) as excitation after passing through a 460 to 490 nm band-pass filter. The excitation intensity under 100x objective was estimated to be 1.3~13.0 W $cm^{-2}$. The signals passed through a 520 nm long-pass filter before collected by a CCD camera (Tucsen, TCH-1.4CICE) and a spectrometer (Renishaw inVia) [7]. The TRPL was normalized and then fitted by a bi-exponential decay function to unveil the carrier transport and recombination dynamics. The color scale bar of TRPL mapping shows the average carrier lifetime.

Transient absorption (TA) spectroscopy measurement

Transient absorption (TA) spectroscopy was performed on a pump probe system (Helios, Ultrafast System LLC). The pulse beam was excited by a Ti:sapphire regenerative amplifier (Legend Elite-1K-HE) and a Nd:YLF laser (EvolutIon 30) pumped. The PVSK films deposited on $SnO_2$, His-$SnO_2$ or NC-$SnO_2$ substrate were excited by a 400 nm laser pulse at the low fluence of 0.6 μJ $cm^{-2}$ to avoid the exciton-exciton and exciton-charge annihilation effects. Data were processed into pseudocolor TAS plots and normalized photobleaching kinetic traces. The normalized photobleaching kinetic traces are fitted with a triple exponential function to obtain the average lifetime of the entire electron quenching process ($\tau_{ave}$)

(Finite-difference time-domain) FDTD method

Compared with other numerical methods, the FDTD can be easy to calculate the distribution of electromagnetic field of arbitrary material and structure [8,9]. So FDTD method [10] is employed to simulate the optical behaviors of near-light-side layer stacks (ITO/$SnO_2$ or NC-$SnO_2$/PVSK). In order to implement the present simulations, the refractive indices (*n*, *k*) of the materials are required. Optical constants of commonly used materials (Glass and ITO) are cited from the reported measurements [11,12]. The refractive index (*n*) and extinction coefficient (*k*) for $SnO_2$, His-$SnO_2$, NC-$SnO_2$ and PVSK ($FA_{0.95}MA_{0.05}PbI_3$) are plotted in Fig. 2(b). It is worth noting that the *n* and *k* value parameters of NC-$SnO_2$ in the FDTD simulation are those of His-$SnO_2$, because the existence of the NC-structure will affect the measurement of the n and k values of the layer by the ellipsometer. This is to avoid the effect of the NC-structure on light being considered twice. In terms of setting the boundary conditions, we use periodic boundary conditions on the x-axis and y-axis and perfectly matched layers on the z-axis. The detailed FDTD simulation parameter settings are listed in Table S1.

Computational method

In this work, all density functional theory (DFT) calculations were performed using the Projection Enhanced Wave (PAW) method, as described in the VASP code

[13]. All structural relaxation and electronic properties were calculated using the Perdew Burke Ernzerhof (PBE) exchange-correlation function [14]. Both the $FAPbI_3$ (001) surface and $SnO_2$ (110) surface were constructed with 15 Å-thick vacuum layer to avoid interactions with the periodic slabs, and the 3×3×1 and 2×2×1 *k*-point meshes in the Brillouin zone were used for optimization of the two structures, respectively. The cutoff energy of 500 eV and the electron energy convergence standard of $1\times10^{-5}$ eV were used as calculation parameters.

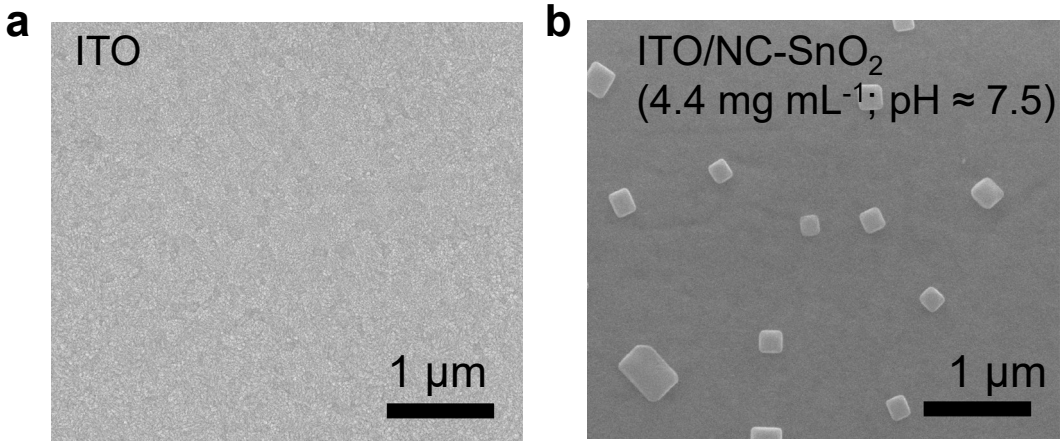


**Supplementary Fig. 1 |** Top-view SEM images of the ITO substrate (**a**) and NC-$SnO_2$ film (**b**), where the NC-$SnO_2$ film was fabricated from a precursor solution (pH ≈ 7.5) containing 4.4 mg $mL^{-1}$ of His-$HCl{\cdot}H_2O$.

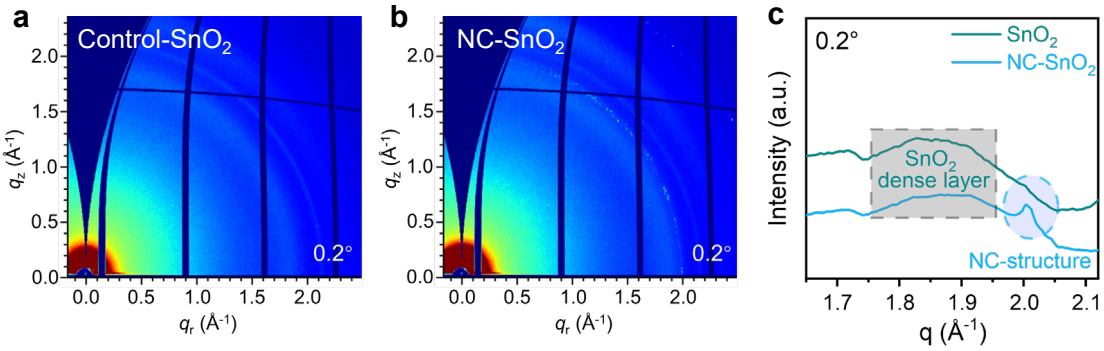


**Supplementary Fig. 2 | GIWAXS characterization of $SnO_2$ films at a 0.2° incident angle. a,** 2D GIWAXS spectra of control-$SnO_2$ film. **b,** 2D GIWAXS spectra of NC-$SnO_2$ film. **c,** 1D GIWAXS profiles for control-$SnO_2$ and NC-$SnO_2$ films.

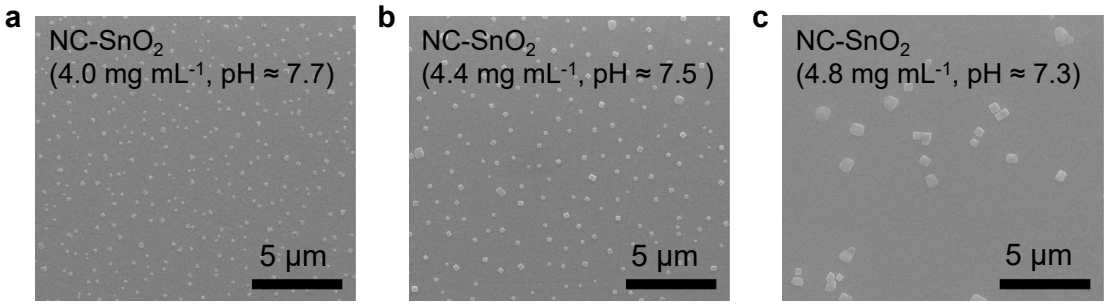


**Supplementary Fig. 3 | Top-view SEM images of NC-$SnO_2$ films prepared from precursor solutions with varying His-HCl·$H_2O$ additive concentrations. a,** Additive concentration of 4.0 mg $mL^{-1}$, corresponding to a solution pH of approximately 7.7. **b,** Additive concentration of 4.4 mg $mL^{-1}$ (pH ≈ 7.5). **c,** Additive concentration of 4.8 mg $mL^{-1}$ (pH ≈ 7.3).

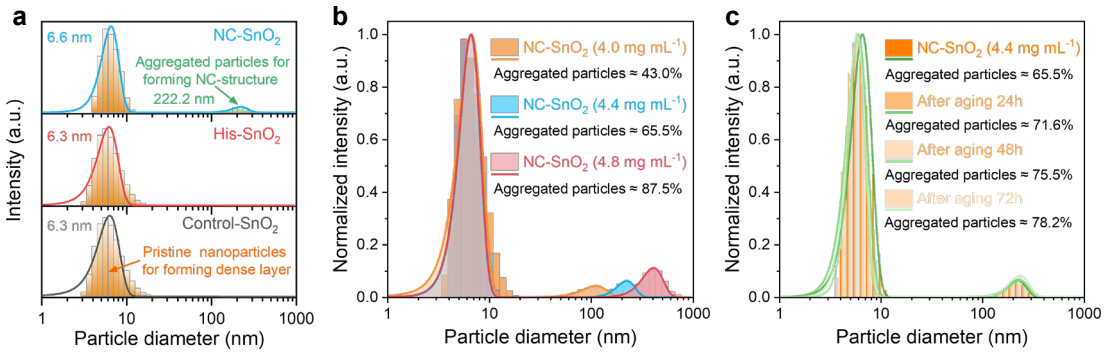


**Supplementary Fig. 4 | DLS analysis of $SnO_2$ colloidal dispersions. a,** The compared particle size distributions for control-$SnO_2$, His-$SnO_2$ and NC-$SnO_2$ colloid dispersion. The bar chart represents the experimentally measured DLS spectra, while the curve corresponds to the Gaussian-fitted normal distribution. **b**, DLS spectra of NC-$SnO_2$ colloidal dispersions at His-$HCl{\cdot}H_2O$ additive concentrations. The number of aggregated particles increases with the additive concentration (corresponding to a decrease in pH), indicating the pH-dependent aggregation behavior. **c**, DLS spectra of NC-$SnO_2$ colloidal dispersions at the optimal additive concentration (4.4 mg $mL^{-1}$) as a function of aging time. With increasing aging time, both the number and size of aggregated particles show a slight increase, but the overall effect remains negligible, indicating that the impact of aging time can be ignored.

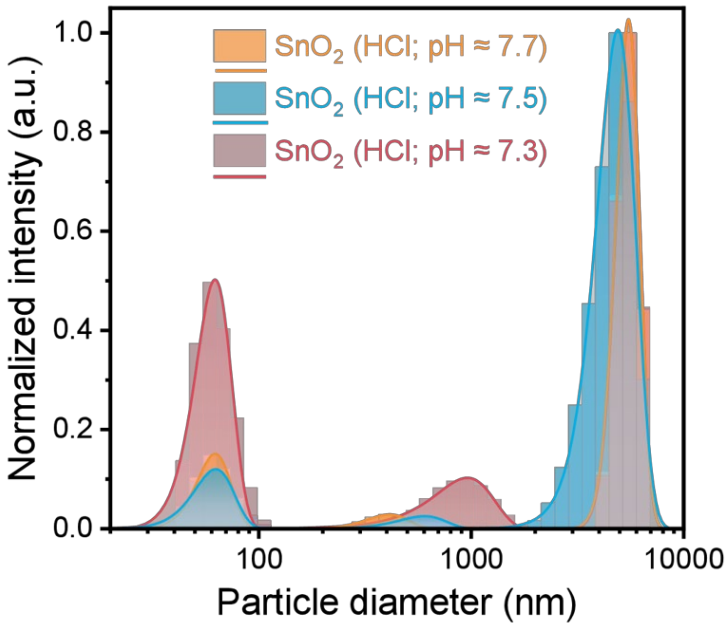


**Supplementary Fig. 5 | DLS analysis of $SnO_2$ colloidal dispersions with pH adjustment by HCl alone.** The compared particle size distributions for commercial $SnO_2$ colloidal dispersions adjusted to target pH using HCl. The bar chart represents the experimentally measured DLS spectra, while the curve corresponds to the Gaussian-fitted normal distribution.

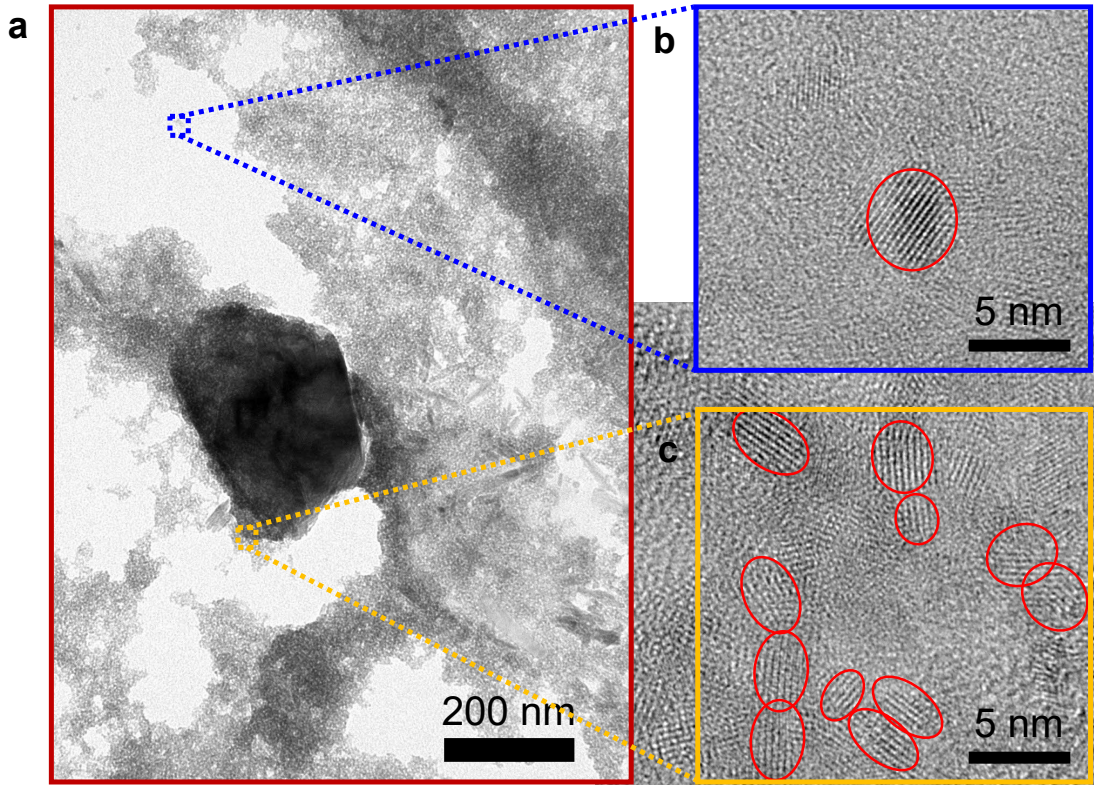


**Supplementary Fig. 6 | TEM image of NC-$SnO_2$ precursor aqueous solution distributed on the copper grid. a,** TEM image at the 200 nm scale showing both small $SnO_2$ nanoparticles and aggregated clusters. **b, c,** High-resolution TEM images of selected regions. Well-dispersed areas reveal small $SnO_2$ nanoparticles (**b**), while significant particle agglomeration is observed at the boundaries of large clusters (**c**).

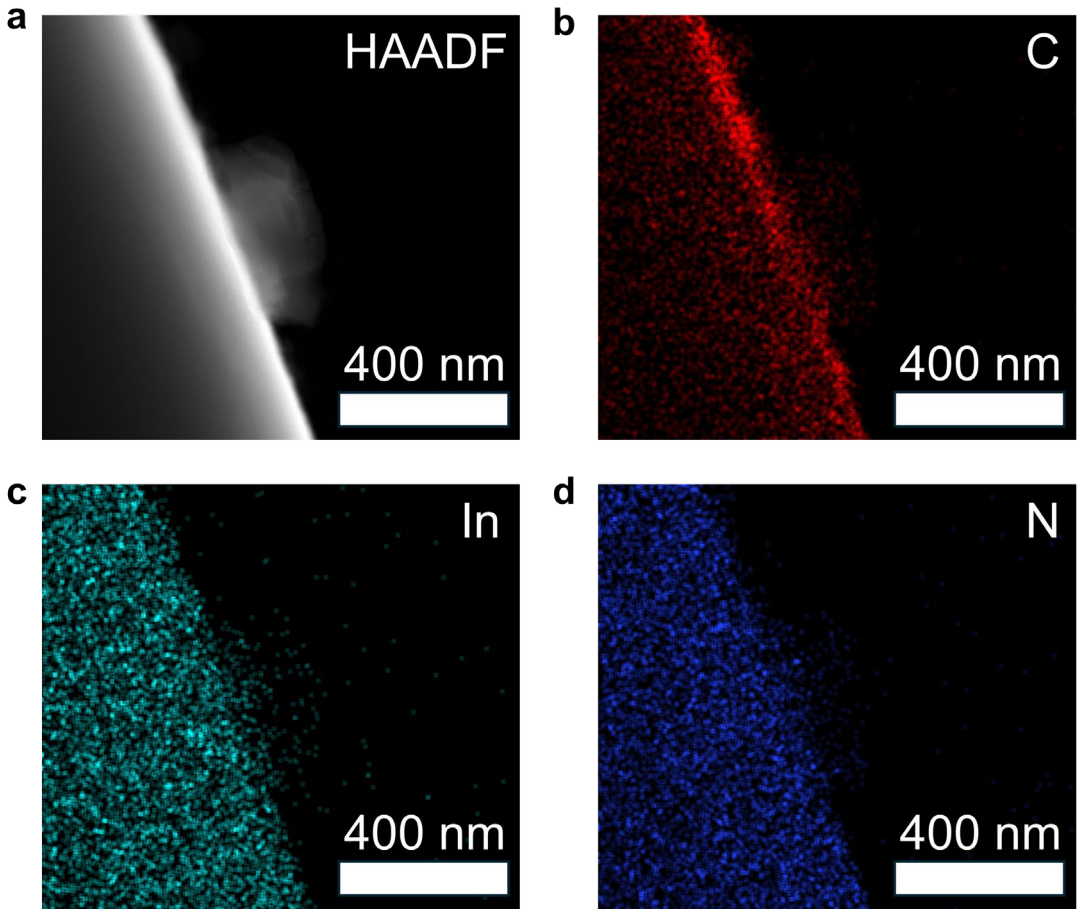


**Supplementary Fig. 7 | Selected area of HAADF-STEM image** of NC-$SnO_2$ on ITO (**a**) and the corresponding STEM-EELS maps of C (**b**), In (**c**), N (**d**) signals. Due to the low content of carboxyl and amino groups in NC-$SnO_2$ after annealing process, these functional groups could not be directly identified by EELS mapping. The uniform distribution patterns of C and N signals are attributed to instrumental noise. To confirm the presence of carboxyl and amino groups in the NC-$SnO_2$ films, Fourier-transform infrared (FTIR) spectroscopy was performed, as shown in **Fig. 3a–d**.

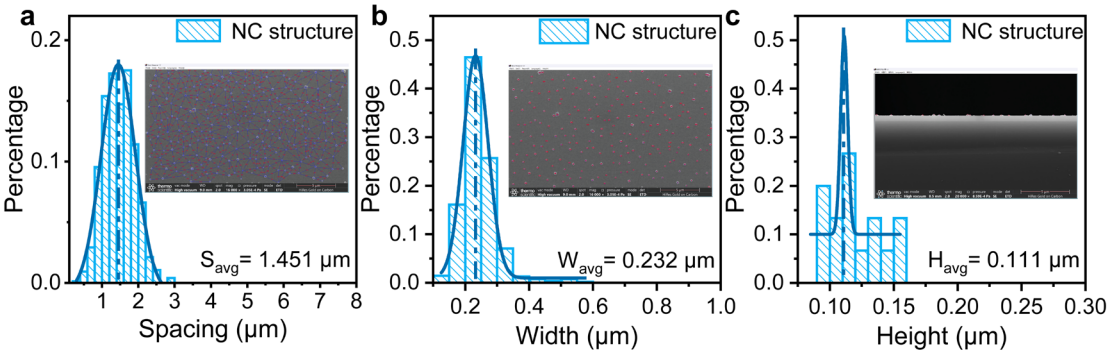


**Supplementary Fig. 8 | Statistical diagram of NC morphology from SEM images.** **a**, Average spacing. **b**, Average width. **c**, Average height. The scale bar represents 1 μm.

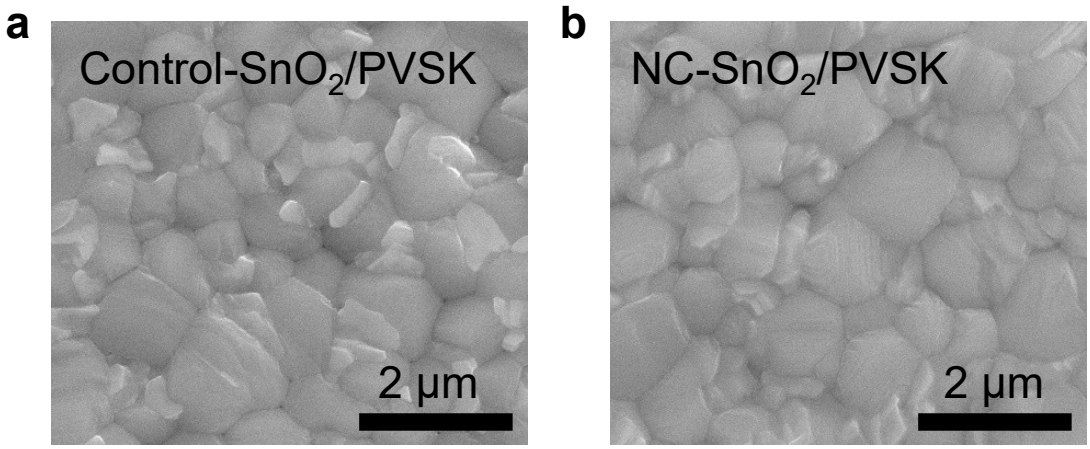


**Supplementary Fig. 9 | SEM images of the air-processed PVSKs grown on** the control-$SnO_2$ (**a**) and NC-$SnO_2$ (**b**).

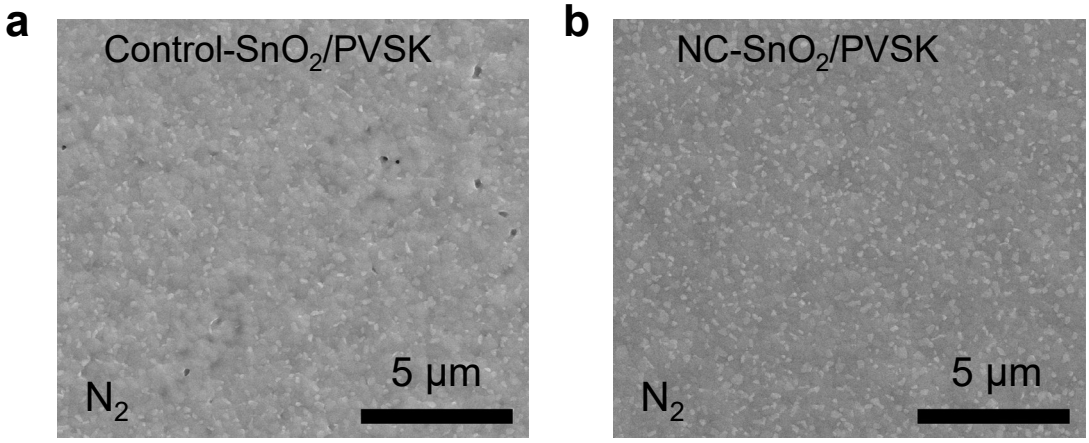


**Supplementary Fig. 10 | SEM images of the $N_2$-processed PVSKs grown on** the control-$SnO_2$ (**a**) and NC-$SnO_2$ (**b**).

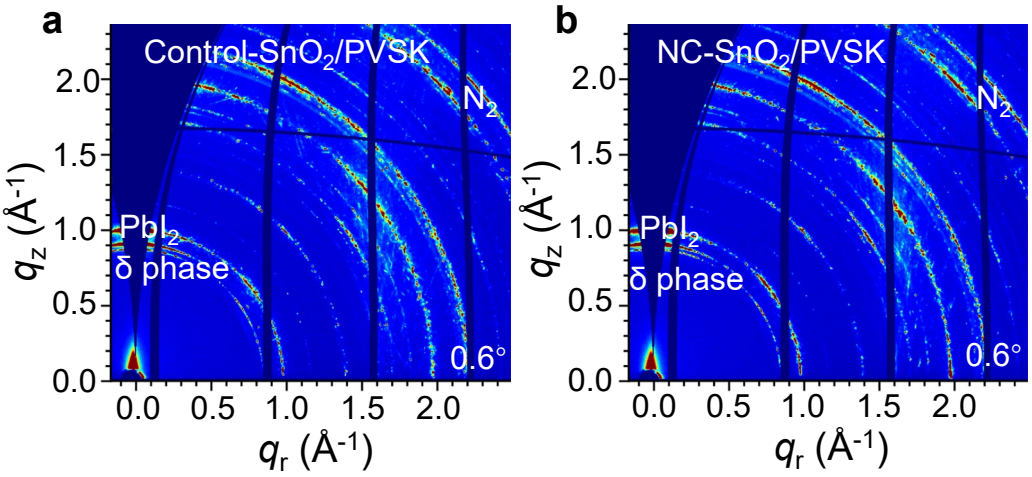


**Supplementary Fig. 11 | GIWAXS patterns of the $N_2$-processed PVSKs grown on** the control-$SnO_2$ (**a**) and the NC-$SnO_2$ (**b**) under $N_2$. The diffraction angle is 0.6°.

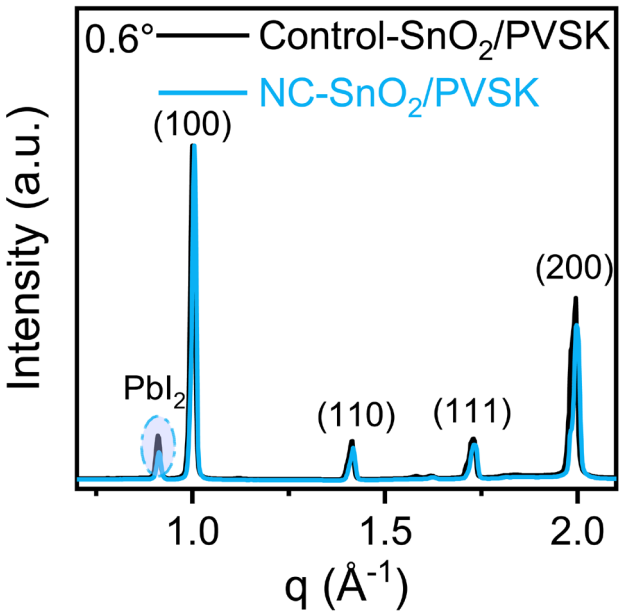


**Supplementary Fig. 12 | 1D GIWAXS profiles for air-processed PVSKs grown on** control-$SnO_2$ and NC-$SnO_2$. The diffraction angle is 0.6°.

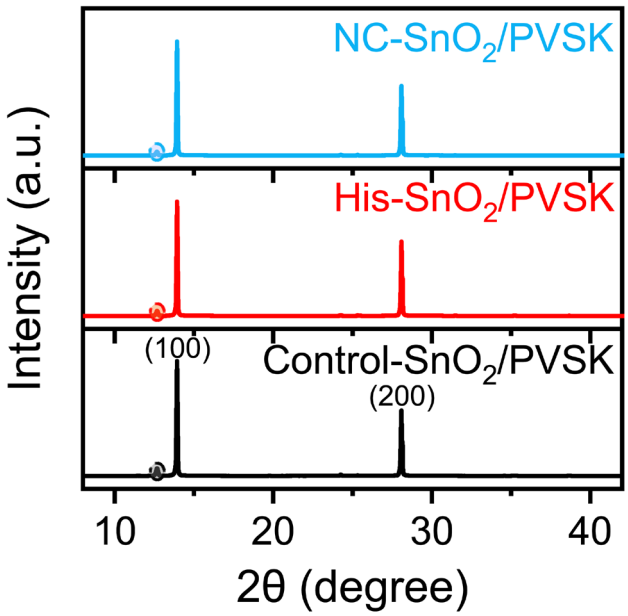


**Supplementary Fig. 13 | XRD patterns of air-processed PVSKs deposited on** control-$SnO_2$, His-$SnO_2$ and NC-$SnO_2$.

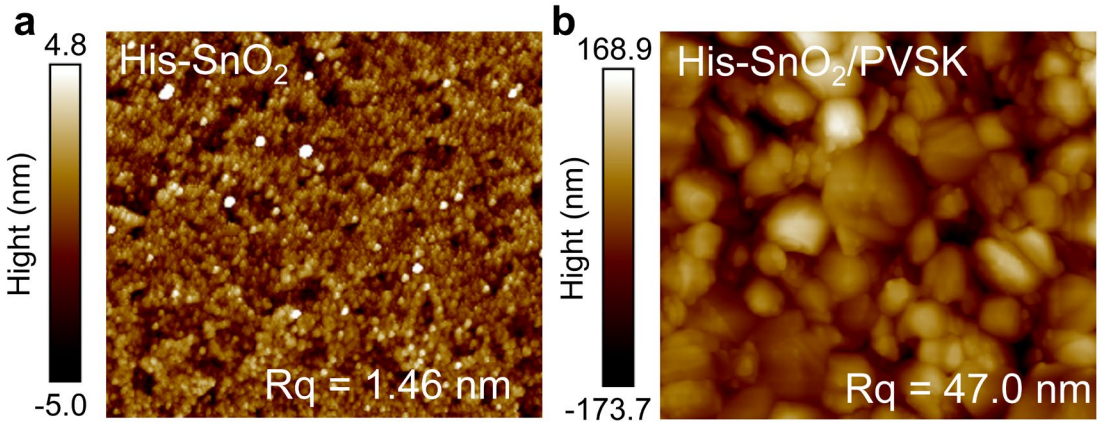


**Supplementary Fig. 14 | AFM images of** the His-$SnO_2$ (**a**), and the His-$SnO_2$/PVSK (**b**).

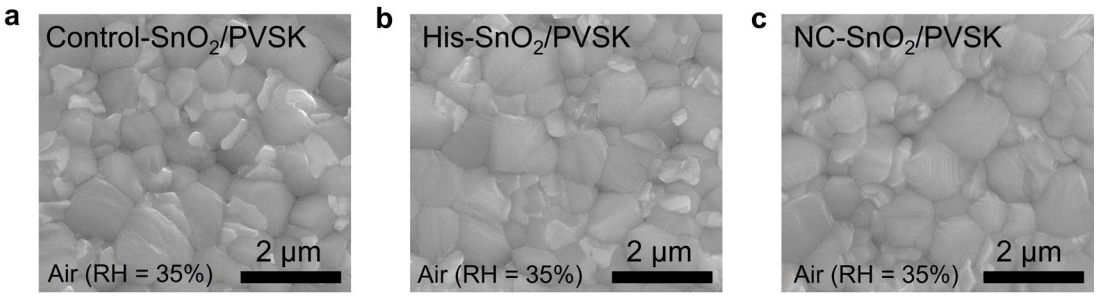


**Supplementary Fig. 15 | SEM images of the PVSK films grown on** the control-$SnO_2$ (**a**), His-$SnO_2$ (**b**) and NC-$SnO_2$ (**c**) under Air (RH=35%). The scale is 2 um.

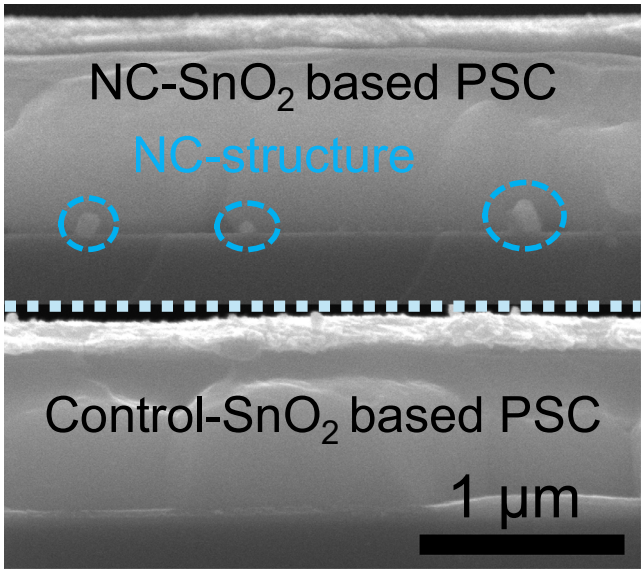


**Supplementary Fig. 16 | Cross-sectional SEM of the PVSK films deposited on** the control-$SnO_2$ and NC- $SnO_2$ films. The scale is 1 um.

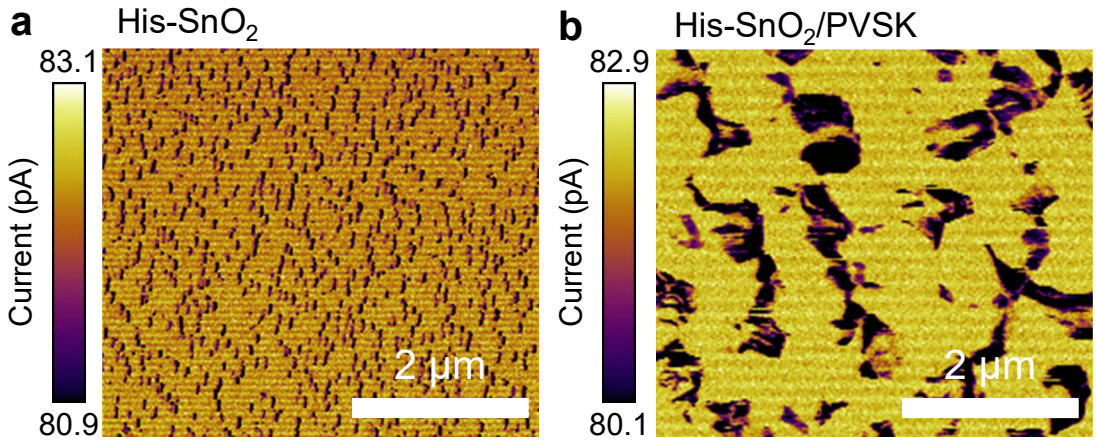


**Supplementary Fig. 17 | c-AFM images of** the His-$SnO_2$ (**a**), His-$SnO_2$/PVSK (**b**).

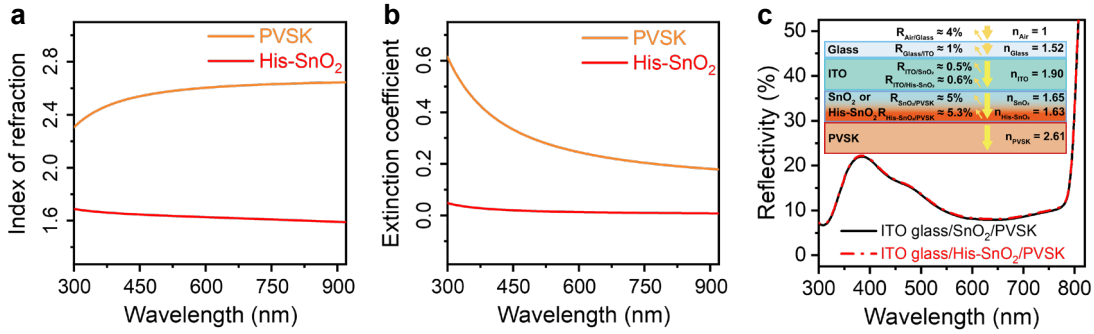


**Supplementary Fig. 18 | The optical analysis of His-$SnO_2$ and PVSK. a**, Refractive index (*n*) of the His-$SnO_2$ and PVSK. **b**, Extinction coefficient (*k*) of the His-$SnO_2$ and PVSK. **c**, Reflectance of interfaces under control-$SnO_2$ and His-$SnO_2$. The reflectivity (*R*) between the interfaces of each layer in ITO/$SnO_2$/PVSK devices, calculated based on *n* and *k*, are shown in the inset of **c**.

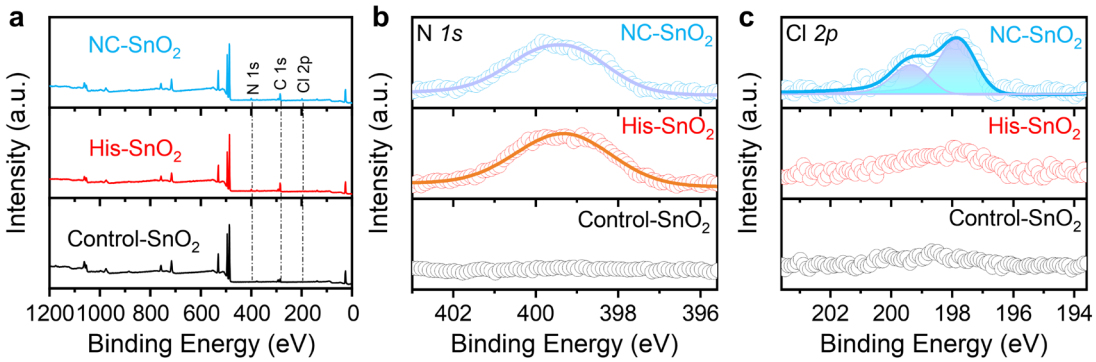


**Supplementary Fig. 19 | XPS spectra for $SnO_2$ samples. a,** XPS survey spectra of control-$SnO_2$, His-$SnO_2$ and NC-$SnO_2$ films. Charging shift compensation was made for both curves using C 1s at 284.8 eV as the reference. Compared with control-$SnO_2$ sample, the His-$SnO_2$ and NC-$SnO_2$ sample clearly revealed peaks from N and Cl, in addition to those from Sn, O, and C. **b,** N 1*s* XPS spectra for control-$SnO_2$, His-$SnO_2$ and NC-$SnO_2$ films. **c,** Cl 2*p* XPS spectra of control-$SnO_2$, His-$SnO_2$ and NC-$SnO_2$ films. The NC-$SnO_2$ film exhibits a higher content of Cl derived from HCl compared to control-$SnO_2$, His-$SnO_2$ films.

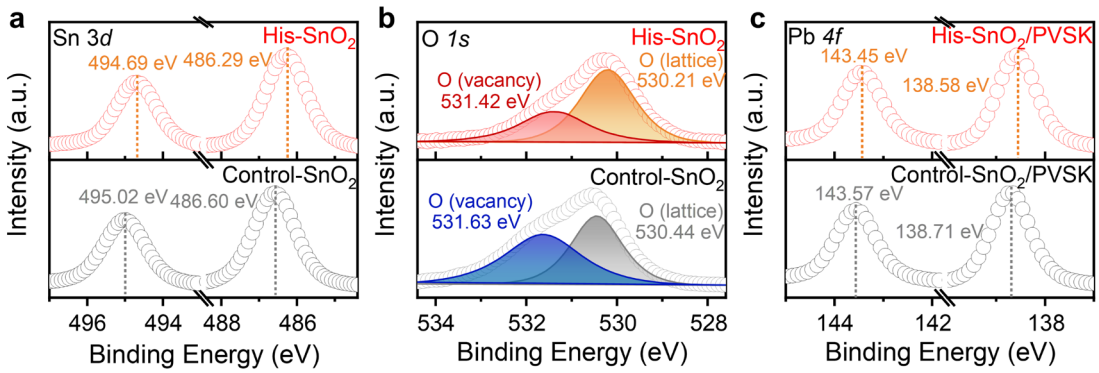


**Supplementary Fig. 20 | Comparison of XPS core-level spectra for control-$SnO_2$ and His-$SnO_2$ films. a,** Sn 3*d* XPS spectra. **b,** O 1*s* XPS spectra. **c,** Pb 4*f* XPS spectra of PVSK films on the control-$SnO_2$ and His-$SnO_2$ films. His-$SnO_2$ and NC-$SnO_2$ share identical functional groups, resulting in similar effects on the passivation of defects in $SnO_2$ and PVSK.

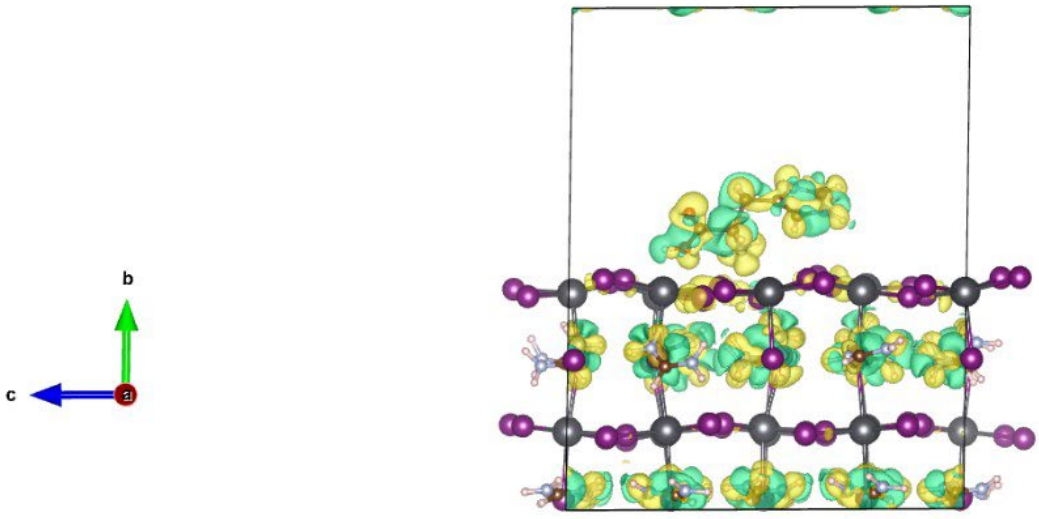


**Supplementary Fig. 21 | The charge density difference of PVSK films with $Pb_I$ antisite defect.** where purple, grey, blue, brown, and pink spheres represent I, Pb, N, C, and H atoms, respectively.

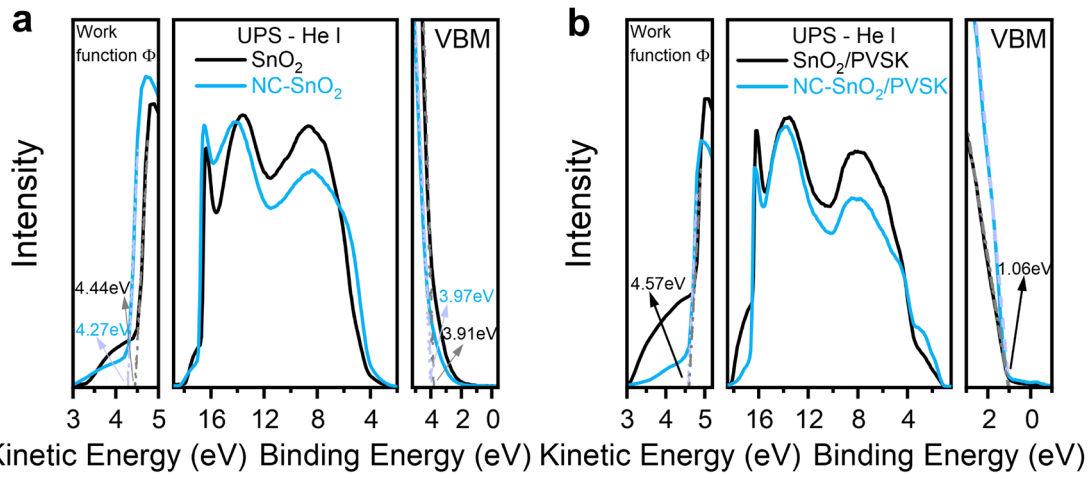


**Supplementary Fig. 22 | UPS spectra** (using the He-I line with photon energy of 21.22 eV) corresponding to the secondary electron onset region (WF, work function) and valence band region (VBM, valence band minimum) of $SnO_2$ and NC-$SnO_2$ films (**a**), $SnO_2$/PVSK and NC-$SnO_2$/PVSK (**b**).

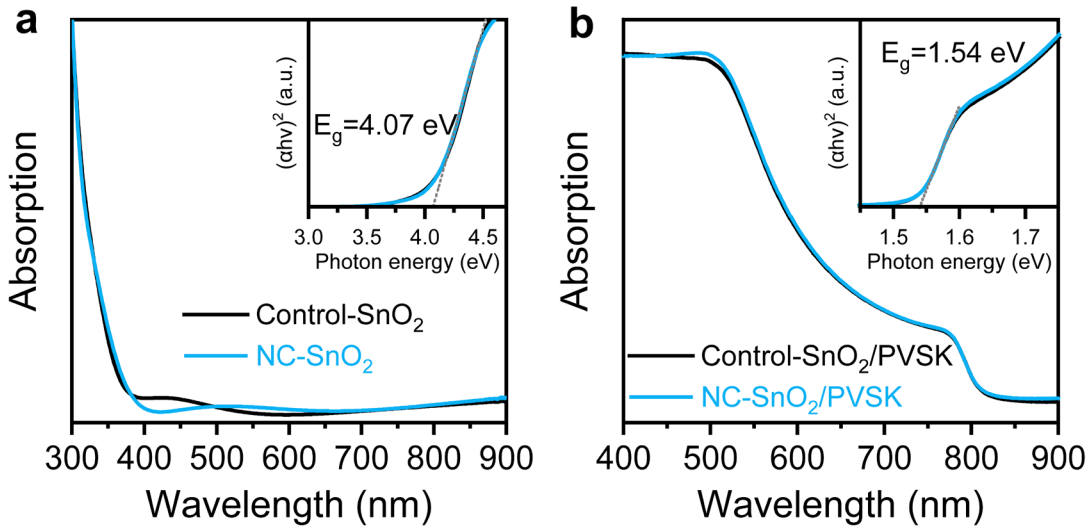


**Supplementary Fig. 23 | Optical absorption properties of $SnO_2$ and $SnO_2$/PVSK.** **a,** UV-vis absorption spectra and the corresponding tauc plots (inset) of the control-$SnO_2$ and NC- $SnO_2$. **b,** UV-vis absorption spectra and the corresponding tauc plots (inset) for PVSK films deposited on control-$SnO_2$ and NC-$SnO_2$. $\alpha$, absorption coefficient; $h$, Planck's constant; $v$, photon's frequency. The dotted lines show the extrapolation of the linear portion of the absorption edges.

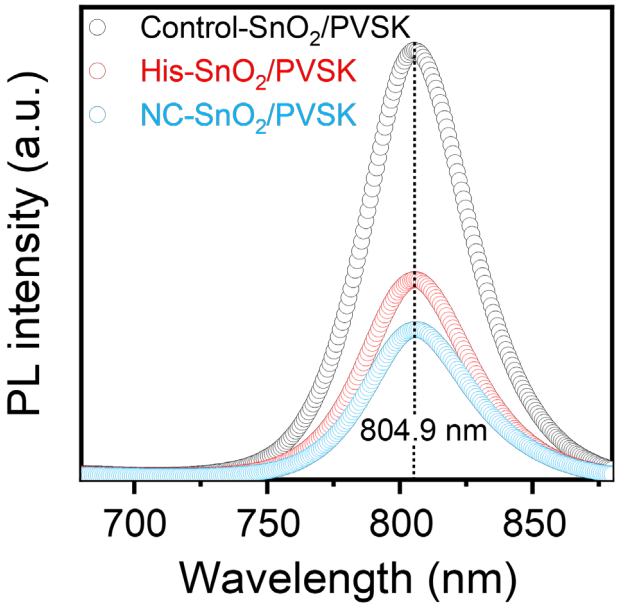


**Supplementary Fig. 24 | PL spectra of the PVSK films deposited on** control-$SnO_2$, His-$SnO_2$ and NC-$SnO_2$. The reduced emission peak (~ 805 nm) intensity near the bandgap confirms the improvement in electron extraction and transport at the bottom interface.

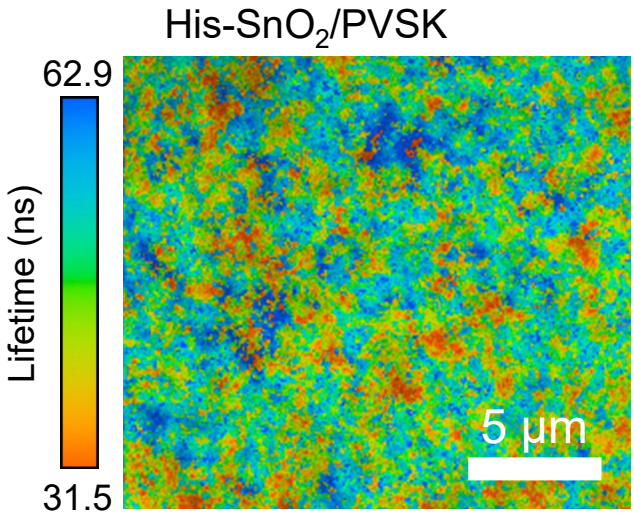


**Supplementary Fig. 25 | TRPL mapping of the PVSK film** on His-$SnO_2$.

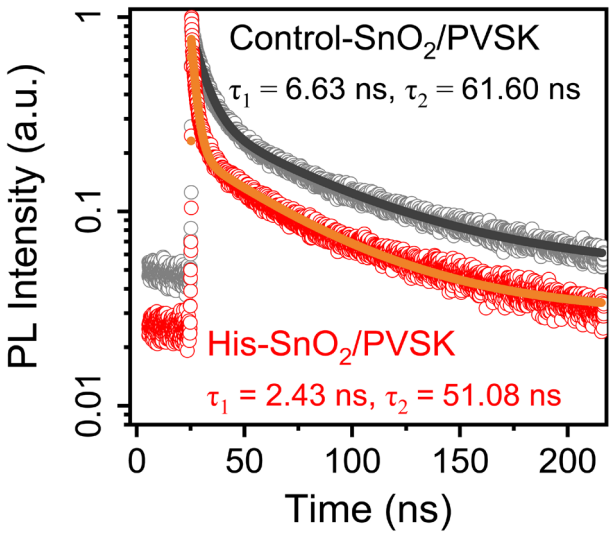


**Supplementary Fig. 26 | Comparison of TRPL decay curves** for the PVSK films on the control-$SnO_2$ and His-$SnO_2$. The decrease in carrier lifetime suggests faster electron extraction and transport at the bottom interface.

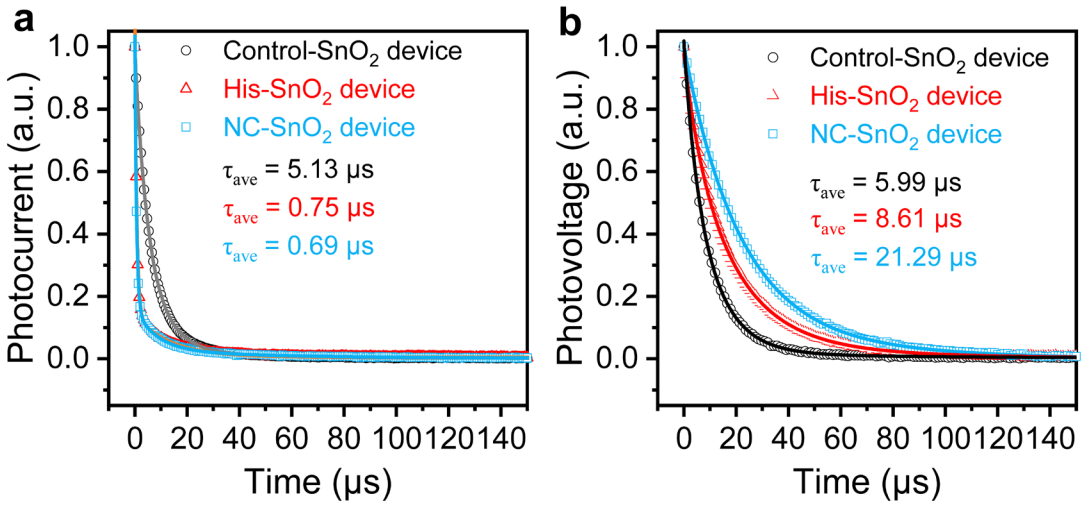


**Supplementary Fig. 27 | TPC and TPV curves for $SnO_2$ ETL-based PSCs. a**, TPC curves of control-$SnO_2$, His- $SnO_2$ and NC- $SnO_2$ ETL-based PSCs. **b**, TPV curves of control-$SnO_2$, His- $SnO_2$ and NC- $SnO_2$ ETL-based PSCs.

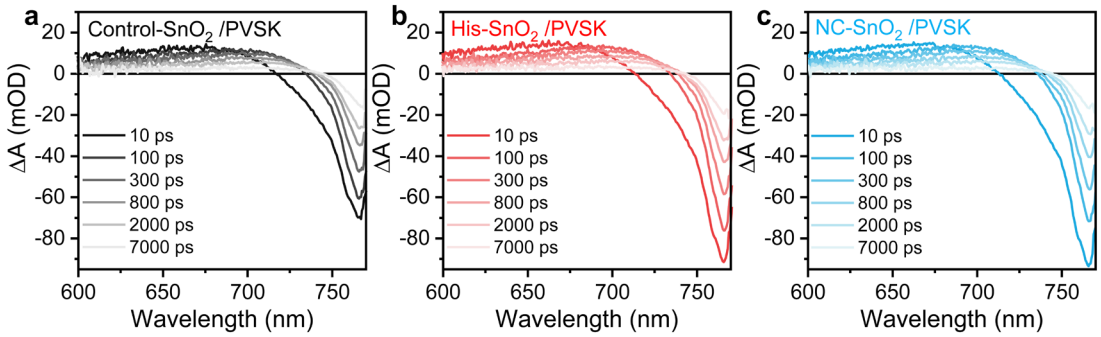


**Supplementary Fig. 28 | Transient TA spectra** of control-$SnO_2$/PVSK (**a**), His-$SnO_2$/PVSK (**b**) and NC-$SnO_2$/PVSK (**c**) excited by 400 nm pump pulse.

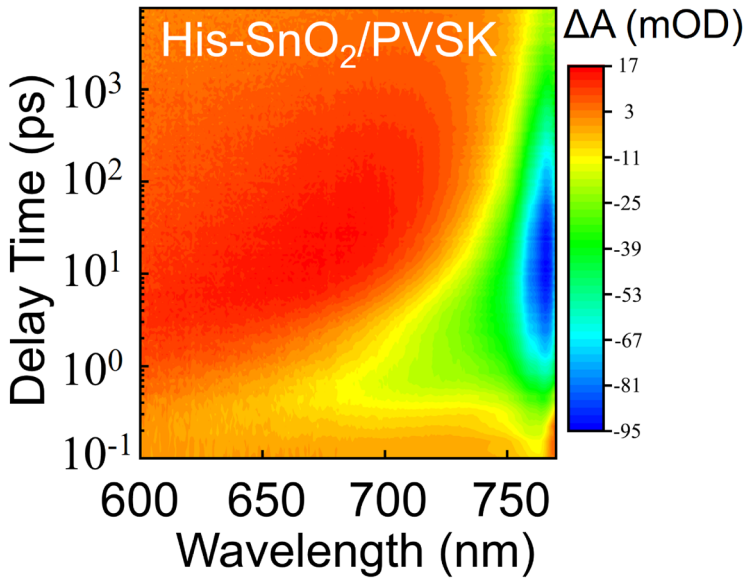


**Supplementary Fig. 29 | The pseudocolor TAS plots** of the PVSK films on His-$SnO_2$.

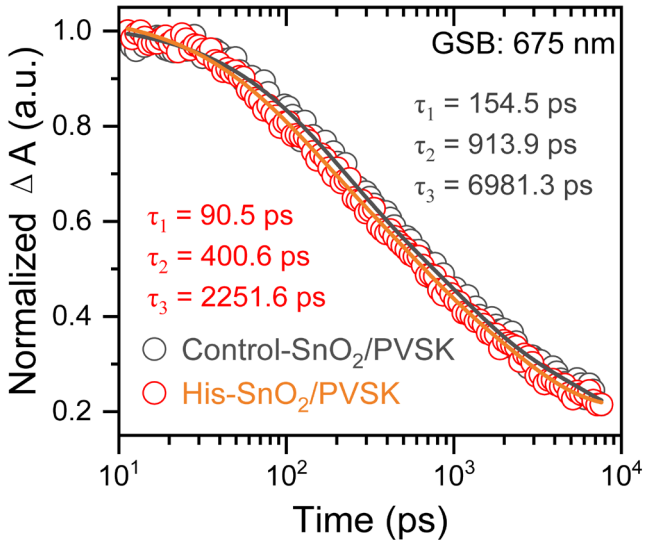


**Supplementary Fig. 30 | Comparison of Normalized photobleaching kinetic traces measured at 765 nm for the PVSK films** on control-$SnO_2$ and His-$SnO_2$. The decrease in carrier lifetime suggests faster electron extraction and transport at the His-$SnO_2$/PVSK interface.

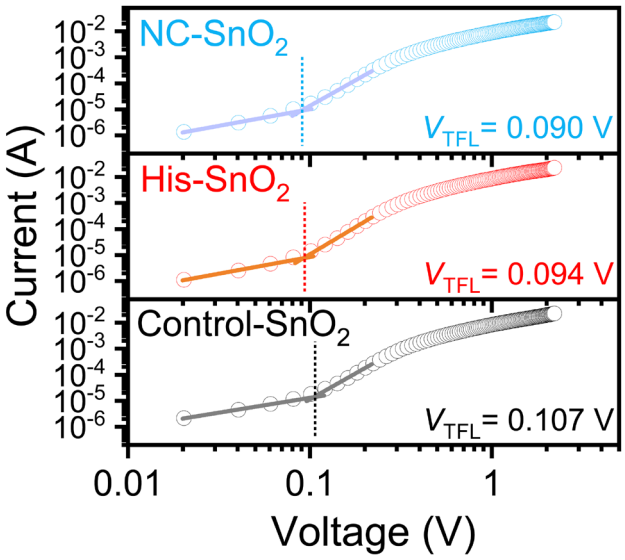


**Supplementary Fig. 31 | Dark *I*-V curves of the electron-only devices based on** the control-$SnO_2$, His- $SnO_2$ and NC- $SnO_2$

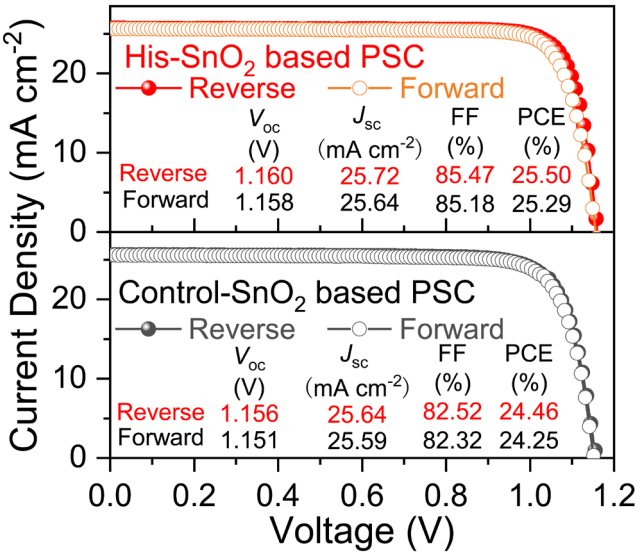


**Supplementary Fig. 32 | Comparison of *J*-V curves and photovoltaic parameters for champion cell** (ITO/Control-$SnO_2$ and His-$SnO_2$/$FA_{0.95}Cs_{0.05}PbI_3$/p-MeOPEAI/Spiro-OMeTAD/Au).

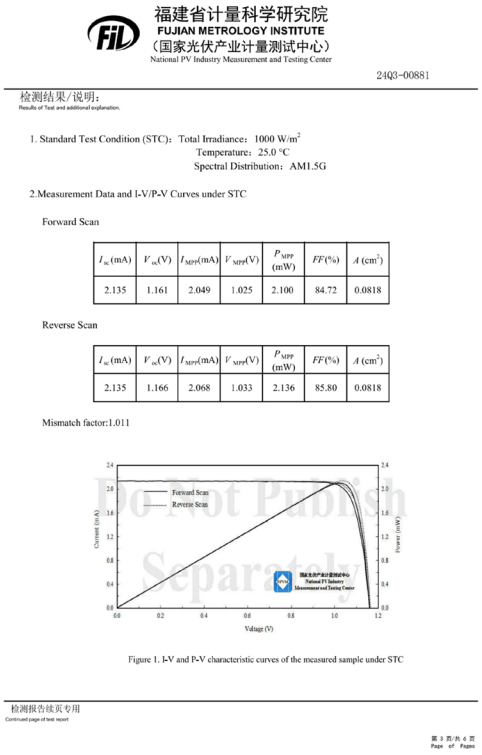

福建省计量科学研究院
FUJIAN METROLOGY INSTITUTE
（国家光伏产业计量测试中心）
National PV Industry Measurement and Testing Center

24Q3-00881

检测结果/说明：
Results of Test and additional explanation.

1. Standard Test Condition (STC)：Total Irradiance：1000 W/m$^2$
Temperature：25.0 ℃
Spectral Distribution：AM1.5G

2.Measurement Data and I-V/P-V Curves under STC

Forward Scan

| $I_{sc}$ (mA) | $V_{oc}$(V) | $I_{MPP}$(mA) | $V_{MPP}$(V) | $P_{MPP}$ (mW) | $FF$(%) | $A$ (cm$^2$) |
|---|---|---|---|---|---|---|
| 2.135 | 1.161 | 2.049 | 1.025 | 2.100 | 84.72 | 0.0818 |

Reverse Scan

| $I_{sc}$ (mA) | $V_{oc}$(V) | $I_{MPP}$(mA) | $V_{MPP}$(V) | $P_{MPP}$ (mW) | $FF$(%) | $A$ (cm$^2$) |
|---|---|---|---|---|---|---|
| 2.135 | 1.166 | 2.068 | 1.033 | 2.136 | 85.80 | 0.0818 |

Mismatch factor:1.011



Figure 1. I-V and P-V characteristic curves of the measured sample under STC



检测报告续页专用
Continued page of test report

第 3 页/共 6 页
Page of Pages

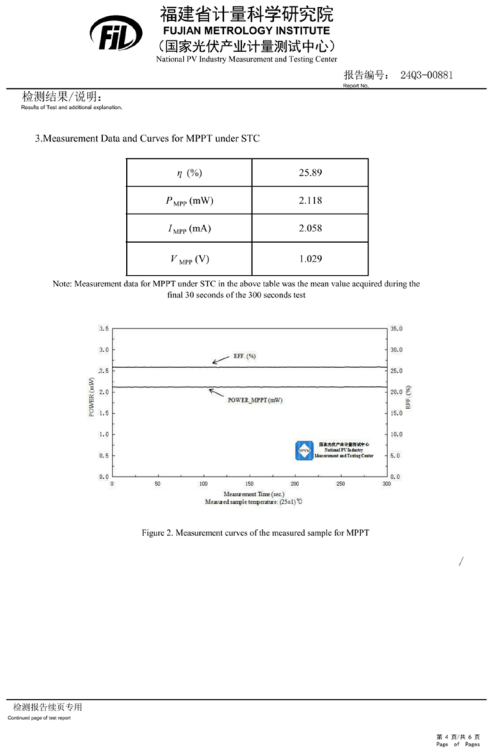

福建省计量科学研究院
FUJIAN METROLOGY INSTITUTE
（国家光伏产业计量测试中心）
National PV Industry Measurement and Testing Center

报告编号： 24Q3-00881
Report No.

检测结果/说明：
Results of Test and additional explanation.

3.Measurement Data and Curves for MPPT under STC

| | |
|---|---|
| $\eta$ (%) | 25.89 |
| $P_{MPP}$ (mW) | 2.118 |
| $I_{MPP}$ (mA) | 2.058 |
| $V_{MPP}$ (V) | 1.029 |

Note: Measurement data for MPPT under STC in the above table was the mean value acquired during the final 30 seconds of the 300 seconds test



Figure 2. Measurement curves of the measured sample for MPPT

/

检测报告续页专用
Continued page of test report

第 4 页/共 6 页
Page of Pages

**Supplementary Fig. 33 | Certification of the NC-$SnO_2$ ETL-based PSC efficiency certified by the NPVM at the Fujian Metrology Institute.** The efficiency was measured with a mask of 0.0818 cm$^2$ aperture area, achieving an $I_{SC}$ of 2.135 mA, $V_{OC}$ of 1.166 V, FF of 85.80% and PCE of 26.11% under reverse scan. The PCE of the maximum power point tracking within 300 seconds was 25.89%.

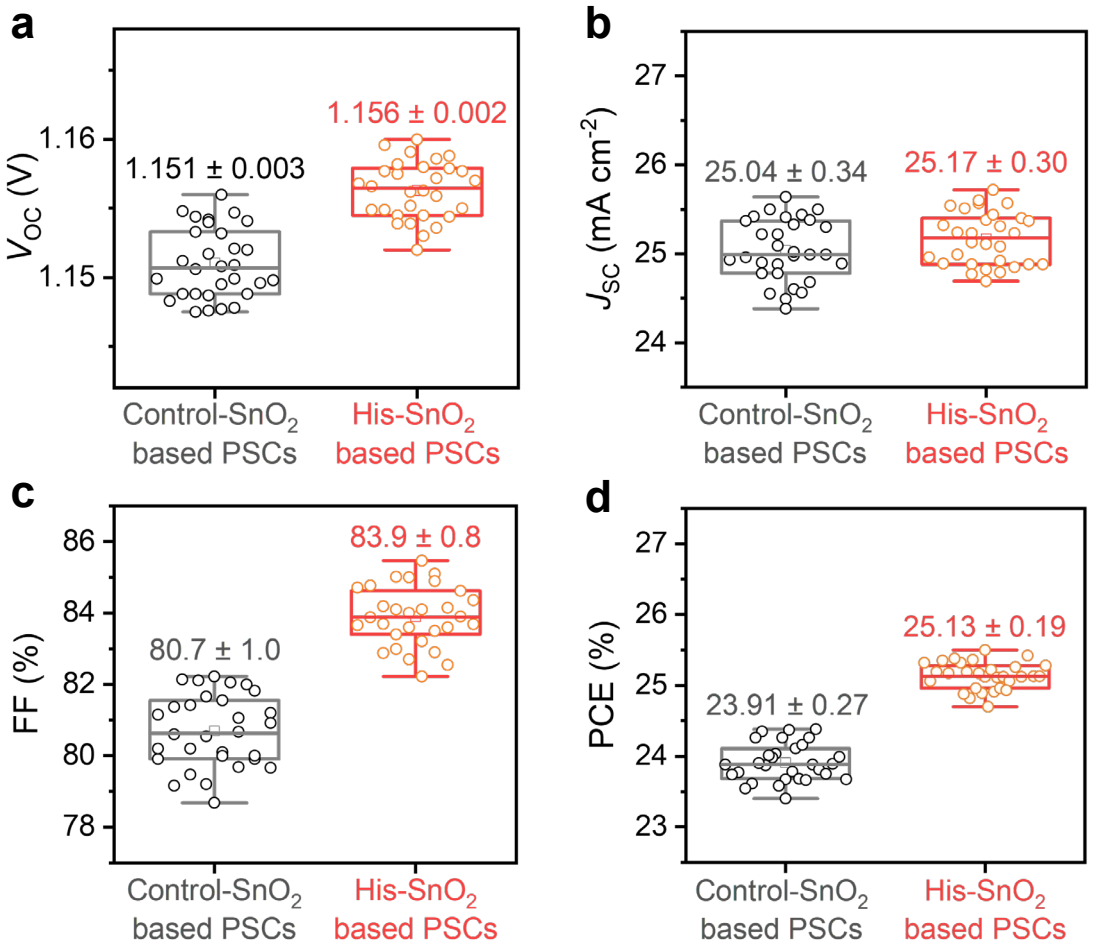


**Supplementary Fig. 34 | Comparison of photovoltaic parameter distribution statistics for 30 devices based on** control-$SnO_2$ and His-$SnO_2$ ETLs, including $V_{OC}$ (**a**), $J_{SC}$ (**b**), FF (**c**) and PCE (**d**).

**Supplementary Table 1 | FDTD simulation parameters of the near-light-side layer stacks.**

| Parameter category | Parameter name | Parameter setting |
|---|---|---|
| structure | ITO | 540nm |
| | Control-$SnO_2$ | 25nm |
| | NC-$SnO_2$ | 25nm |
| | NC structures | **Supplementary Fig.8** |
| | PVSK | 600nm |
| FDTD simulation region settings | Mesh accuracy | 2 |
| | Mesh type | Auto non-uniform |
| | Mesh refinement | Conformal variant 1 |
| | PML type | Uniaxial anisotropic PML |
| | Time step dt stability factor | 0.99 (unitless) |
| | Time step dt | 0.0087 fs |
| | Minimum mesh step | 0.25 nm |
| | Simulation time | 3000 fs |
| Plane wave source settings | Source shape | Plane wave |
| | Amplitude | 1 (Normalized) |
| | Phase | 0° |
| | Polarization angle | 0° |
| | Plane wave type | Bloch/periodic |
| | Time domain pulse type | Broad band |
| | Time domain frequency | 666.21 THz |
| | Pulse length | 1.99 fs |
| | Offset | 5.66 fs |
| | Band width | 666.21 THz |

**Supplementary Table 2 | The fitted delays lifetimes of TA kinetics.**

| Sample | $A_1$ (%) | $\tau_1$ (ps) | $A_2$ (%) | $\tau_2$ (ps) | $A_3$ (%) | $\tau_3$ (ps) |
|---|---|---|---|---|---|---|
| Glass/ITO/control-$SnO_2$/PVSK | 31.38 | 154.46 | 32.92 | 913.87 | 23.22 | 6981.27 |
| Glass/ITO/His-$SnO_2$/PVSK | 23.57 | 90.54 | 27.64 | 400.56 | 32.14 | 2251.62 |
| Glass/ITO/NC-$SnO_2$/PVSK | 29.88 | 79.94 | 27.11 | 387.84 | 28.97 | 2157.39 |

**Supplementary Table 3 | Summary of recently reported air-prepared and light management PSCs.**

| Reported air-prepared PSCs | | | | | | |
|---|---|---|---|---|---|---|
| **Year** | **RH (%)** | **Perovskites** | **Types** | **PCE (%)** | **Area ($cm^2$)** | **Ref.** |
| 2021 | ~40 | $Cs_{0.01}FA_{0.94}MA_{0.05}PbI_{2.85}$ | n-i-p | 22.06 | 0.09 | 15 |
| 2023 | ~40 | $FA_xMA_{1-x}PbI_3$ | n-i-p | 22.40 | 0.09 | 16 |
| 2023 | 30±5 | $FA_xMA_{1-x}PbI_3$ | n-i-p | 23.30 | / | 17 |
| 2023 | 30~40 | $FAPbI_3$ | n-i-p | 24.00 | 0.09 | 18 |
| 2023 | 30~85 | $FA_xMA_{1-x}PbI_3$ | n-i-p | 25.03 | 0.08 | 19 |
| 2024 | 20~30 | $FA_xMA_{1-x}PbI_3$ | n-i-p | 24.16 | 0.09 | 20 |
| 2024 | / | $FA_xMA_{1-x}PbI_3$ | n-i-p | 24.63 | / | 21 |
| 2024 | 20~60 | $FAPbI_3$ | n-i-p | 24.70 | 0.09 | 22 |
| 2024 | 20~50 | $FAPbI_3$ | n-i-p | 25.08 | 0.04 | 23 |
| 2024 | ~30 | $MA_{0.7}FA_{0.3}PbI_3$ | p-i-n | 25.10 | 0.0684 | 24 |
| 2024 | / | $FAPbI_3$ | n-i-p | 24.42 | / | 25 |
| 2024 | / | $(FA_{0.95}Cs_{0.05})_{0.98}Rb_{0.02}Pb(Br_{0.03}Cl_{0.06}I_{2.91})$ | n-i-p | 25.13 | / | 26 |
| 2024 | 15~25 | $Cs_{1-x}(FAMA)_xPb(I_xBr_{1-x})_3$ | n-i-p | 25.18 | 0.09 | 27 |
| 2024 | 35~50 | $Cs_{1-x}(FAMA)_xPb(I_xBr_{1-x})_3$ | p-i-n | 25.11 | 0.06 | 28 |
| 2025 | ~60 | $Cs_{1-x}(FAMA)_xPb(I_xBr_{1-x})_3$ | p-i-n | 25.20 | 0.046 | 29 |
| 2025 | 20~40 | $FAPbI_3$ | p-i-n | 25.05 | 0.09 | 30 |
| 2025 | 20~80 | $Rb_{1-x}(FAMA)_xPb(I_xBr_{1-x})_3$ | n-i-p | 25.10 | 0.0805 | 31 |
| 2025 | 30-40 | $MA_{0.7}FA_{0.3}PbI_3$ | p-i-n | 26.00 | 0.08 | 32 |
| **2025** | **~35** | $FA_{0.95}Cs_{0.05}PbI_3$ | **n-i-p** | **26.22** | **0.0557** | **This work** |

| Reported light management PSCs | | | | |
|---|---|---|---|---|
| **Year** | **Optimization** | **Perovskites** | **PCE (%)** | **Ref.** |
| 2015 | Perovskite thickness | **$MAPbI_3$** | 16.5 | 33 |
| 2019 | Perovskite thickness | **$MAPbI_3$** | 18.4 | 34 |
| 2019 | Texturing PTAA | **$MAPbI_3$** | 20.8 | 35 |
| 2021 | Perovskite thickness | **$FAPbI_3$** | 25.59 | 36 |
| 2023 | Texturing substrates | **$Cs_{0.05}MA_{0.1}FA_{0.85}PbI_3$** | 25.3 | 37 |
| 2024 | Additional antireflection | **$FAPbI_3$** | 23.83 | 5 |
| 2025 | Texturing substrates | **$Cs_{1-x}(FAMA)_xPb(I_xBr_{1-x})_3$** | 26.4 | 38 |
| **2025** | Texturing $SnO_2$ | **$FA_{0.95}Cs_{0.05}PbI_3$** | **26.22** | **This work** |

**Reference**


1. Deng, Y. *et al.* Defect compensation in formamidinium–caesium perovskites for highly efficient solar mini-modules with improved photostability. *Nat. Energy* **6**, 633-641 (2021).
2. Park, N.-G. & Zhu, K. Scalable fabrication and coating methods for perovskite solar cells and solar modules. *Nat. Rev. Mater.* **5**, 333-350 (2020).
3. Zhang, X. *et al.* Low-cost and large-scale producible biomimetic radiative cooling glass with multiband radiative regulation performance. *Adv. Opt. Mater.* **10**, 2202031 (2022).
4. Zhou, Z., Wang, X., Ma, Y., Hu, B. & Zhou, J. Transparent polymer coatings for energy-efficient daytime window cooling. *Cell Rep. Phys. Sci.* **1**, 100231 (2020).
5. Dai, Q. *et al.* Highly reliable anti-reflection radiative cooling glass applicable to thermal management of solar cells. *Chem. Eng. J.* **498**, 155768 (2024).
6. Yang, Z. & Zhang, J. Bioinspired radiative cooling structure with randomly stacked fibers for efficient all-day passive cooling. *ACS Appl. Mater. Interfaces* **13**, 43387-43395 (2021).
7. Li, Z. *et al.* Beyond the phase segregation: probing the irreversible phase reconstruction of mixed-halide perovskites. *Adv. Sci.* **9**, e2103948 (2022).
8. Tiguntseva, E. *et al.* Resonant silicon nanoparticles for enhancement of light absorption and photoluminescence from hybrid perovskite films and metasurfaces. *Nanoscale* **9**, 12486-12493 (2017).
9. Yin, J. *et al.* Light absorption enhancement by embedding submicron scattering $TiO_2$ nanoparticles in perovskite solar cells. *RSC Adv.* **6**, 24596-24602 (2016).
10. FDTD solutions. https://www.lumerical.com (2025).
11. Xing, G. *et al.* Low-temperature solution-processed wavelength-tunable perovskites for lasing. *Nat. Mater.* **13**, 476-480 (2014).
12. Ball, J. M. *et al.* Optical properties and limiting photocurrent of thin-film perovskite solar cells. *Energy Environ. Sci.* **8**, 602-609 (2015).
13. Blochl, P. E. Projector augmented-wave method. *Phys. Rev. B: Condens. Matter.* **50**,

17953-17979 (1994).

14. Perdew, J. P., Burke, K. & Ernzerhof, M. Generalized gradient approximation made simple. *Phys. Rev. Lett.* **78**, 1396-1396 (1997).
15. Jung, K. *et al.* Ambient-air fabrication of stable mixed cation perovskite planar solar cells with efficiencies exceeding 22% using a synergistic mixed antisolvent with complementary properties. *Nano Energy* **89**, 106387 (2021).
16. Zhang, W. *et al.* Multiple roles of negative thermal expansion material for high-performance fully-air processed perovskite solar cells. *Chem. Eng. J.* **457**, 141216 (2023).
17. Zeng, Q. *et al.* Tailoring particle size of $PbI_2$ towards efficient perovskite solar cells under ambient air conditions. *Chem. Commun.* **59**, 5269-5272 (2023).
18. Du, Y. *et al.* Crystallization control based on the regulation of solvent-perovskite coordination for high-performance ambient printable $FAPbI_3$ perovskite solar cells. *Adv. Mater.* **36**, e2307583 (2024).
19. Yan, L. *et al.* Fabrication of perovskite solar cells in ambient air by blocking perovskite hydration with guanabenz acetate salt. *Nat. Energy* **8**, 1158-1167 (2023).
20. Tian, C. *et al.* Anion-stabilized precursor inks toward efficient and reproducible air-processed perovskite solar cells. *Adv. Energy Mater.* **14**, 2303666 (2024).
21. Liu, B. *et al.* Polydentate ligand reinforced chelating to stabilize buried interface toward high-performance perovskite solar cells. *Angew. Chem. Int. Ed.* **63**, e202317185 (2024).
22. Zou, Y. *et al.* A crystal capping layer for formation of black-phase $FAPbI_3$ perovskite in humid air. *Science* **385**, 161-167 (2024).
23. Shi, X. *et al.* Air-Processed perovskite solar cells with >25% efficiency and high stability enabled by crystallization modulation and holistic passivation. *Adv. Mater.* **36**, e2402785 (2024).
24. Wang, S. *et al.* Lead-chelating intermediate for air-processed phase-pure $FAPbI_3$ perovskite solar cells. *Angew. Chem. Int. Ed.* **136**, e202407192 (2024).
25. Zhou, Q. *et al.* Managing photons and carriers by multisite chiral molecules

achieving high-performance perovskite solar cells fabricated in ambient air. *Nano Energy* **124**, 109512 (2024).

26. Yang, H. *et al.* Iodide management and oriented crystallization modulation for high-performance all-air processed perovskite solar cells. *Adv. Mater.* **36**, e2411721 (2024).
27. Tian, C. *et al.* Air-processed efficient perovskite solar cells with full lifecycle management. *Adv. Mater.* **37**, e2411982 (2025).
28. Meng, H. *et al.* Inhibition of halide oxidation and deprotonation of organic cations with dimethylammonium formate for air-processed p-i-n perovskite solar cells. *Nat. Energy* **9**, 536-547 (2024).
29. Xu, L. *et al.* In situ cation exchange enables air-processed inverted perovskite solar cells with over 25% efficiency and enhanced stability. *Angew. Chem. Int. Ed.*, e202503702(2025).
30. Wu, G. *et al.* Two-step inverted perovskite solar cells with >25% efficiency fabricated in ambient air. *Adv. Energy Mater.*, 2500830, (2025).
31. Zhang, Y. *et al.* Solvent environment engineering for reliable fabrication of perovskite solar cells in air with a wide humidity range. *Adv. Energy Mater.*, 2500156 (2025).
32. Liu, T. *et al.* Efficient perovskite solar modules enabled by a UV-stable and high-conductivity hole transport material. *Sci. Adv.* **11**, eadu3493, (2025).
33. Lin, Q., Armin, A., Nagiri, R. C. R., Burn, P. L. & Meredith, P. Electro-optics of perovskite solar cells. *Nat. Photon.* **9**, 106-112 (2014).
34. Liu, Y. *et al.* Efficiency of $MAPbI_3$-based planar solar cell analyzed by its thickness-dependent exciton formation, morphology, and crystallinity. *ACS Appl. Mater. Interfaces* **11**, 14810-14820 (2019).
35. Xu, C. Y. *et al.* Coordinated optical matching of a texture interface made from demixing blended polymers for high-performance inverted perovskite solar cells. *ACS Nano* **14**, 196-203 (2020).
36. Jeong, J. *et al.* Pseudo-halide anion engineering for alpha-$FAPbI_3$ perovskite solar cells. *Nature* **592**, 381-385 (2021).

37. Park, S. M. *et al.* Low-loss contacts on textured substrates for inverted perovskite solar cells. *Nature* **624**, 289-294 (2023).
38. Ge, Y. *et al.* Suppressing wide-angle light loss and non-radiative recombination for efficient perovskite solar cells. *Nat. Photon.* **19***,* 170-177 (2025).